optics

Article

Blue-Noise-Based Disordered Photonic Structures Show Isotropic and Ultrawide Band Gaps

Edoardo De Tommasi , Silvia Romano and Gianluigi Zito *

Institute of Applied Sciences and Intelligent Systems, National Research Council, Via P. Castellino 111, I-80131 Naples, Italy; edoardo.detommasi@cnr.it (E.D.T.); silvia.romano@cnr.it (S.R.)
* Correspondence: gianluigi.zito@cnr.it

Abstract: Spatially disordered but uniformly distributed point patterns characterized by so-called blue-noise long-range spatial correlations are of great benefit in computer graphics, especially in spatial dithering thanks to the spatial isotropy. Herein, the potential photonic properties of blue-noise disordered, homogeneous point processes based on farthest-point optimization are numerically investigated for silicon photonics. The photonic properties of blue-noise two-dimensional patterns are studied as a function of the filling fraction and benchmarked with photonic crystals with a triangular lattice. Ultrawide and omnidirectional photonic band gaps spanning most of the visible spectrum are found with estimates of gap–midgap ratios of up to 55.4% for transverse magnetic polarization, 59.4% for transverse electric polarization, and 32.7% for complete band gaps. The waveguiding effect in azimuthal defect lines is also numerically evaluated. These results corroborate the idea that long-range correlated disordered structures are helpful for engineering novel devices with the additional degree of freedom of spatial isotropy, and capable of bandgap opening even without total suppression of infinite-wavelength density fluctuations.

Keywords: photonic bandgap; blue-noise disorder; near-hyperuniform disorder

check for updates

Citation: De Tommasi, E.; Romano, S.; Zito, G. Blue-Noise-Based Disordered Photonic Structures Show Isotropic and Ultrawide Band Gaps. *Optics* **2023**, *4*, 573–583. https://doi.org/10.3390/opt4040042

Academic Editors: Thomas Seeger and Clare C. Byeon

Received: 4 September 2023
Revised: 18 October 2023
Accepted: 31 October 2023
Published: 3 November 2023

1. Introduction

Photonic technologies benefit from the availability of broad spectral ranges at which light propagation is inhibited, especially in the visible spectral range, for instance to increase light extraction efficiency in ultra-low-threshold semiconductor lasers [1,2], light-emitting diodes [3], or perovskites thin films [4]. The existence and engineering of suitable light stopbands is at the foundation of photonic crystals (PhCs) [5,6], in which the geometry and symmetries of the dielectric arrangement determine most of the overall properties of the system.

Many kinds of periodic, quasi-periodic, and aperiodic photonic structures [7–9] have been designed, aiming at maximizing the gap–midgap ratio $\Delta\omega/\omega_c$ ($\Delta\omega$ = stopband width, ω_c = center frequency) for increasing the operational spectral range; and achieving omnidirectional light stopbands capable of waveguiding light along complex embedded paths. For two-dimensional periodic PhCs, a hexagonal arrangement of circular columns connected to their nearest neighbors by slender rectangular rods allows obtaining a complete (i.e., blocking all directions and polarizations of light) photonic band gap (PBG), characterized by a theoretical value of $\Delta\omega/\omega_c$ of 24.2% by a proper choice of r/a and d/a ratios, where r is the radius of the columns, d is the width of the slender rods, and a is the lattice constant [10]. It can be shown that the structures that maximize the width of a PBG between bands n and $n+1$ in a two-dimensional PhC can be obtained starting from the minimum-energy distribution of n points in the unit cell satisfying symmetry and periodicity of the crystal [11]. In turn, these n points correspond to the center of n high refractive index dielectric cylinders that ensure the quasi-optimal PBG for transverse magnetic (TM) polarization. A proper tessellation [12] based on the same points defines a partition of the unit cell into n subdomains whose walls constitute the quasi-optimal structure for transverse electric (TE) polarization. For a relative permittivity $\epsilon_r = 11.56$ of the high index material (silicon) in air, values of $\Delta\omega/\omega_c$ of 48% have been reported for TM polarization and hexagonal close-packed (HCP) arrangement of cylinders, and 50% for TE polarization and HCP-tiled air inclusions into a high index material, assuming a Voronoi tessellation [6,11].

Rotational symmetries higher than 6-fold (HCP case) aim at omnidirectional stopbands, which can be employed to embed waveguides with complex pathways in the confining photonic environment. In this direction, a higher spatial isotropy associated with quasi-crystalline configurations (e.g., 8-, 10-, 12-fold rotational symmetry) [13–17] introduces an important advance. Florescu et al. [18] designed an optimization scheme that allows obtaining, for 5-fold symmetric quasicrystals (10-fold rotational symmetry) composed of silicon and air, values of $\Delta\omega/\omega_c$ of 39%, 42.3%, and 16.5% for TM, TE, and complete PBGs, respectively.

It is interesting that biological structures such as *Lepidiota stigma* and *Cyphochilus* sp. white beetles are characterized by high reflectance in all the visible spectrum [19] (a PBG property) that is associated with a disordered morphology at the nanoscale, because of a certain degree of homogeneity and spatial correlation [20]. On the other hand, randomly disordered Poisson patterns are perfectly isotropic but lack the mutual spatial correlation to engineer the scattering suppression at the basis of stopbands. In this direction, a few years ago, *hyperuniformity* metrics was introduced to describe a material configuration that is characterized by disordered isotropic patterns with a high degree of homogeneity on the large scale, i.e., long-range spatial correlation capable of inducing the distinctive interference proper of a PBG [18,21–25]. Hyperuniform disorder corresponds, in reciprocal space, to an azimuthally averaged structure factor, $S(k)$, that tends to zero with a specific behavior as the wavenumber $k = |\mathbf{k}|$ tends to zero, which implies that infinite wavelength density fluctuations vanish because of spatial correlation [21,26,27]. Indeed, disordered hyperuniform point patterns have been employed to design highly homogeneous and isotropic two-dimensional photonic structures characterized by the presence of omnidirectional PBGs with gap–midgap ratios of 36.5% and 29.6% for TM and TE polarizations, respectively [22,28].

In the field of computer graphics, the general class of blue-noise disordered (BND) patterns was also introduced to achieve point spatial distributions capable of providing the highest quality in printed and digital images [29]. The use of point distributions characterized by uniformity (average point density approximately constant) but disorder to guarantee isotropy (absence of symmetries or regular structures) is indeed of great benefit in computer graphics, especially in spatial dithering, when the illusion of continuous-tone pictures on displays that are capable of only binary elements is requested [30]. These peculiarities are associated with blue noise, i.e., the density fluctuations (noise) are suppressed at low spatial frequencies (large length scale) [31]. Distributions characterized by blue noise are distinguished by homogeneous mutual distances between points and no apparent regularity artifacts, allowing the generation of good-quality digital halftones [32]. In the Fourier domain, blue noise implies that the spectral energy is low in a circular disk around the origin (as a consequence of the wide mutual spacing of points) and the energy varies smoothly outside this disk due to the disorder of the distribution [29]. In contrast to Poisson point processes characterized by white noise in the reciprocal space, BND patterns possess only short wavelength noise.

Now, we can recognize that the main attribute of hyperuniform disorder is in that the structure factor shows long-range fluctuations that are totally suppressed with a well-defined scaling law, and thus only short-range fluctuations—blue noise—are allowed. Thereby, hyperuniform disordered point distributions are a very specific type of blue-noise patterns requiring precise engineering of spatial correlations since hyperuniformity can be destroyed by point displacement [33,34]. In addition, no complete PBGs have been observed for finite levels of infinite-wavelength density fluctuations [22]. To the best of our knowledge, removing this stringent constraint by investigating photonic applications for the more general class of blue-noise patterns with finite levels of infinite-wavelength density fluctuations, as used in computer graphics, has not been reported yet.

Here, therefore, we studied a kind of uniform and irregular point distribution based on the *farthest-point optimization* algorithm [29]. In particular, we found that this specific disordered structure is capable of supporting ultrawide, omnidirectional band gaps covering most of the visible spectrum, and benchmarked the results against the HCP lattice. The presence of complete PBGs and the possibility to design waveguides with an arbitrary bending angle is also discussed.

2. Results

2.1. Farthest-Point Optimization Algorithm for Blue-Noise Disorder Design

The *farthest-point optimization* (FPO) method was introduced by Schlömer et al., in order to compute a BND pattern with good spatial isotropy [29]. This iterative method enlarges the minimum reciprocal distance between points of a random set, thus improving the blue-noise characteristics of the ensemble, starting from a Poisson point distribution. Given a random set, X, of $n = ||X||$ points and starting from the distance $d_T(x, y)$ based on toroidal metrics between points x and y, the following definitions hold:

$$d_x = \min_{y \in X \setminus \{x\}} d_T(x, y) \tag{1}$$

$$\bar{d}_X = \frac{1}{n} \sum_{x \in X} d_x \tag{2}$$

$$d_{max} = \left(\frac{2}{\sqrt{3}n} \right)^{\frac{1}{2}} \tag{3}$$

$$\bar{\delta}_X = \frac{\bar{d}_X}{d_{max}} \tag{4}$$

where d_x is the *local* minimum distance, $\bar{d}_X$ is the *average* minimum distance, d_{max} is the *largest* minimum distance (obtained for a hexagonal lattice), and $\bar{\delta}_X$ is the normalized average minimum distance. In brief, a single step of the algorithm consists of moving each point, x, of the ensemble to a new position that is as far away from the remaining points as possible, thus increasing $\bar{\delta}_X$. In practice, before moving it, each point, x, is removed from the Delaunay triangulation (DT) of the remaining points, $X \setminus \{x\}$. The remaining triangles are inspected in order to find the farthest point, f, which is finally reinserted as a new point in the DT, which is thus updated during the iteration until convergence. This procedure converges as $n \log n$; the algorithm is implemented with MathWorks Matlab 2022 (Natick, MA, USA), and convergence time is of the order of seconds. Other iterative methods aimed at the maximization of the average minimum distance between points often converge towards locally regular patterns [35], failing to obtain blue-noise distributions, or are costly in terms of time per iteration (typically converging as n^2), and, moreover, lead to values of $\bar{\delta}_X$ not significantly higher than those obtained by non-iterative methods [32].

In Figure 1a–d, HCP and BND point patterns from FPO with relative structure factor maps are reported for comparison. As it can be seen, the structure factor of the BND pattern, unlike that of an ordered, hexagonal distribution of points, shows a high level of isotropy, and thus it lacks changes in the spatial occurrence of points along different directions. A look at the azimuthally averaged structure factor, $S(k)$, for the BND pattern reveals the lower density fluctuations at low spatial frequencies (Figure 1e). In this sense, the BND pattern can be considered as a near-hyperuniform disordered structure since $S(k) < 0.1$ for a spatial frequency below 0.1 in normalized units. It is worth mentioning that ideal hyperuniformity is a property of infinitely large systems [36] but the structure factor asymptotic scaling can be evaluated in finite patterns fitting the variance number $\sigma_N^2(R) = a\,R^2 + b\,R\ln(R) + c\,R$, as a function of the pattern size in normalized units $R = R_D/L$, according to refs. [27,37], where R_D is the radius of the sampling disk and L is the side size of the square pattern. The fitting coefficients found for the FPO BND pattern were $\{a, b, c\} = \{0.005, 0.24, 0.52\}$ with a Pearson's coefficient of $R_p^2 = 0.9964$ (see Figure S1 in Supplementary Materials). The suppression of the quadratic term in the fit and the dominant surface-term scaling $c > b$ provide indication of large spatial correlations, a near-hyperuniformity since $a = S(k = 0) = 5 \times 10^{-3}$, but without ideal hyperuniformity ($a = 0$). It is thus significant to evaluate whether a PBG can be achieved via the BND FPO pattern. Indeed, it must be noted that, in Ref. [22], no complete PBGs were observed for finite $a = S(k = 0)$, and PBGs opened only for zero fluctuations within a finite disk of wavevectors in the reciprocal space, i.e., $S(k) = 0$, for $k < k_C = R_C/L$, where R_C is some critical radius value. Finding complete PBGs in the FPO BND pattern could be interesting both from a fundamental point of view and for practical applications given the simplicity of the calculation, as for instance for the realization of efficient isotropic thermal radiation sources and the fabrication of waveguides characterized by an arbitrary bending angle. Therefore, we will now evaluate the existence of the PBG and compare the results with the HCP case, which represents the most performing pattern in terms of the PBG, yet is anisotropic (hampering designing free-form defect pathways).

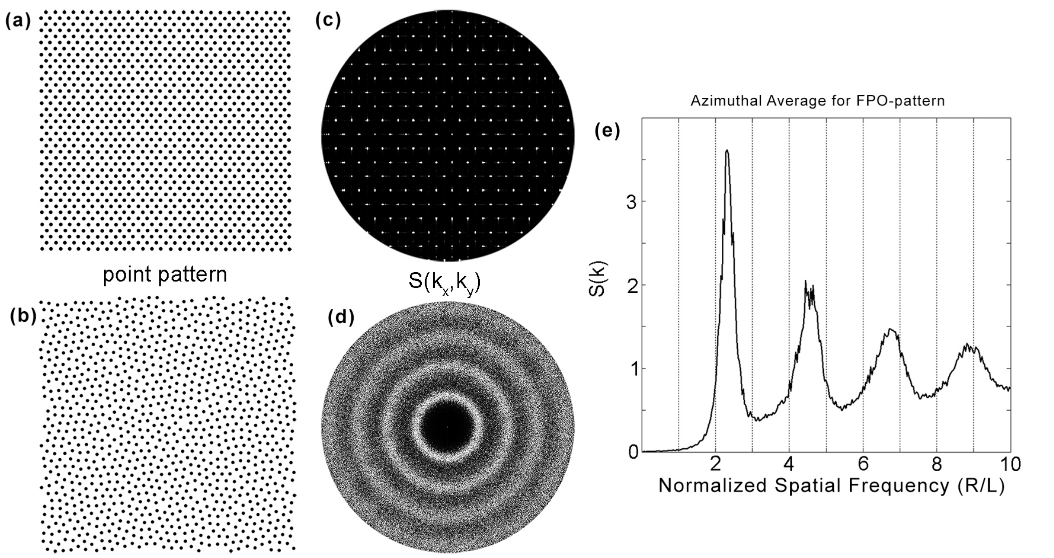

Figure 1. Hexagonal close-packed (HCP) (**a**) and blue-noise disordered (BND) (**b**) point patterns with relative structure factor maps (**c**,**d**). The BND pattern has been obtained with farthest-point optimization [29] after 63 iterations, starting from a random set of $n = 1024$ points (see text). In (**e**), the azimuthally averaged structure factor, $S(k)$, relative to the BND point pattern is reported, showing the suppression of density fluctuations at low spatial frequencies.

2.2. Photonic-Band-Gap Analysis of Farthest-Point Optimization Pattern

At each point of the FPO distribution, a cylinder of a given material was placed, as characterized by a radius, r, and a normalized average minimum distance with respect to its neighbors, $\bar{\delta}_X = a$. We investigated the onset of PBGs and compared the results with HCP patterns as a function of the refractive index of the materials and filling fraction ratio, r/a. All numerical simulations were based on the finite difference time domain (FDTD) method, as detailed below.

For what concerns the FPO finite structure that lacks periodicity, Maxwell's equations were solved using the FDTD method in FullWAVE, Rsoft CAD Photonics Suite environment, Synopsys [38]. The discretization grid provided a minimum of 16 grid points per unit length a for basic analyses, then up to 64 grid points for fine futures. It is not possible to define a Brillouin zone in a nonperiodic structure like our FPO pattern since the Wigner–Seitz cell in the direct space changes point by point. Therefore, for the disordered patterns we used a near-field dipole source with a short-pulse temporal decay profile (Gaussian time pulse excitation) to excite the modes of the system and calculate the local density of states and associated band gap. The source point was placed at the center of the structure generally, but also outside the boundaries of the pattern for a further consistency check. The ramp time was $0.03(\lambda/c)$ in order to have a pulse wide enough to cover the range of wavelengths of interest (in-plane wavevector modulus). In order to detect the radiation transmitted through the dielectric pattern and radiating outside of the structure in free space, field monitors were placed in a set of positions inside and outside the pattern at different orientations with respect to the center. The discrete positions were selected to cover 30 in-plane scattering wavevectors directions in a disk around the center of the pattern. Field components and power flows along different propagation directions were stored. After a sufficiently large time of calculation (typically $2^{17}\Delta t$, where Δt is the FDTD time step given by 0.5 d_g, where d_g is the grid size), the field was Fourier transformed to calculate the transmission spectrum along specific directions, as also discussed in previously reported methods [17].

For what concerns HCP patterns, due to the periodicity of this structure, dispersion curves and PBGs were retrieved by means of the plane wave expansion technique (BandSOLVE, Rsoft CAD Photonics Suite environment, Synopsis [39]). This means that the structure is virtually infinite and associated PBGs are likely to be overestimated with respect to a real-world finite structure.

HCP Pattern: TM case. PBG properties of HCP structures are a gold standard in photonic applications. Data of PBGs (gap–midgap ratio) are shown as a function of the r/a ratio, together with the trends of the band gap boundary wavelengths λ_1 and λ_2, for the refractive index difference $\Delta n = 3.4$, which is compatible with high index cylinders of materials like Ge, $MoSe_2$, MoS_2, and others in air in the visible spectral range (when neglecting absorption losses). The comparison will be then evaluated for other values of Δn compatible with other materials like silicon (n = 4.09 at 550 nm) for the FPO pattern in the following. It is worth mentioning that neglecting the absorption loss at this stage does not affect the outcome from the comparison between the patterns, since simulations are indeed made with the same materials as a function only of the spatial arrangement of the cylinders. The specific choice of the real part of the refractive index is the same for both patterns as well. As can be seen in Figure 2a, the best performance in terms of the gap–midgap ratio for TM polarization takes place for $r/a = 0.15$, with $\Delta\omega/\omega_c = 59.2\%$, spanning a spectral range from $\lambda_1 = 476$ nm to $\lambda_2 = 877$ nm. At same time, a full-visible spectrum for TM polarization occurs around $r/a = 0.13$.

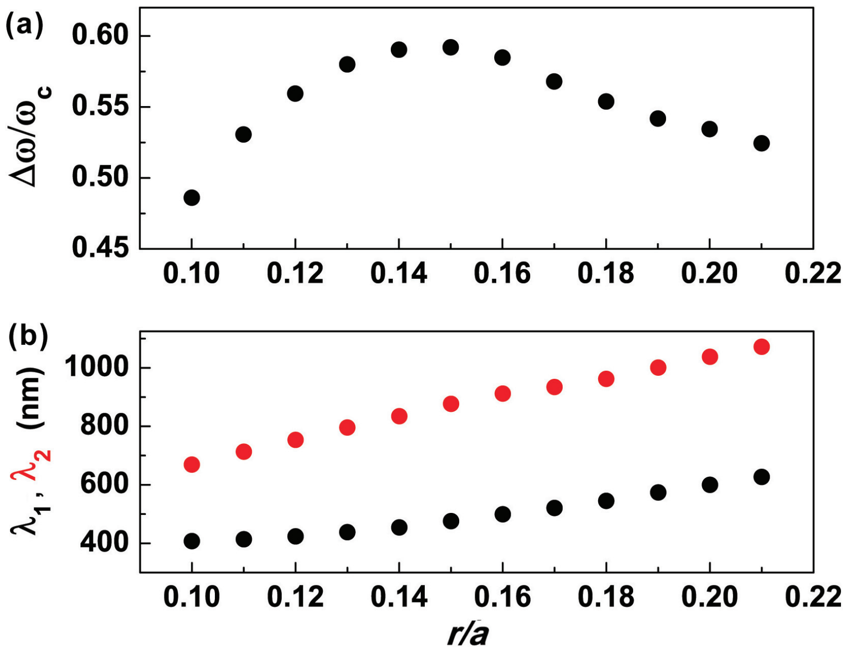

Figure 2. Gap–midgap ratio (**a**) and band gap boundary wavelengths (**b**) as a function of the r/a ratio for an HCP distribution of cylinders with a refractive index contrast of $\Delta n = 3.4$ with respect to the environment. The simulations have been performed for TM polarization.

However, the spatial *anisotropy* associated with the order and symmetry of the structure has some drawbacks. For finite structures, the unavailability of real isotropic PBGs in periodic PhCs may be noticeable, hampering the possibility of fabricating waveguides with an arbitrary bending angle [40]. The PBG completeness will be addressed later for convenience.

FPO Pattern: TM case. The FPO pattern response can be seen in Figure 3, in which the values of the gap–midgap ratio for TM polarization, for three values of refractive index difference decreasing from $\Delta n = 3.4$, are shown as a function of the r/a ratio, together with the trends of the band gap boundary wavelengths λ_1 and λ_2. The best performance is reached for $\Delta n = 3.4$. In particular, when $r/a = 0.12$, a PBG characterized by $\Delta\omega/\omega_c = 55.4\%$ and spanning from 384 to 678 nm takes place. This value overcomes the performances of the other *isotropic* disordered or quasi-ordered photonic structures introduced so far. Furthermore, for $r/a = 0.13$, the PBG spans all the visible spectrum (406–706 nm), still being characterized by a noticeable value of $\Delta\omega/\omega_c$, which in this case equals 54% (see Figure 4). It is worth mentioning that, while the gap-to-midgap ratio can be scaled to any range of frequency, the right panels show the actual extreme wavelengths obtained considering an average spacing a = 220 nm. This also means that the wavelength to the desired range of interest, λ_f, can be obtained by scaling the spacing according to $a' = a \times \lambda_f/\lambda_i$, where λ_i is the initial midgap wavelength shown in our specific calculation. Let us consider Figure 3b right panel, case Δn = 2.4, i.e., $\sqrt{12} - \sqrt{1}$ = silicon refractive index (NIR)—air refractive index, with r/a = 0.19, which shows a PBG ranging from 425 to 650 nm, with midgap wavelength $\lambda_i = 540$ nm. To move from λ_i = 540 nm of this representative case to a final wavelength λ_f = 1500 nm in the NIR (midgap wavelength), it is only necessary to scale the spacing according to $a' = 220 \times 1500/540 = 610$ nm.

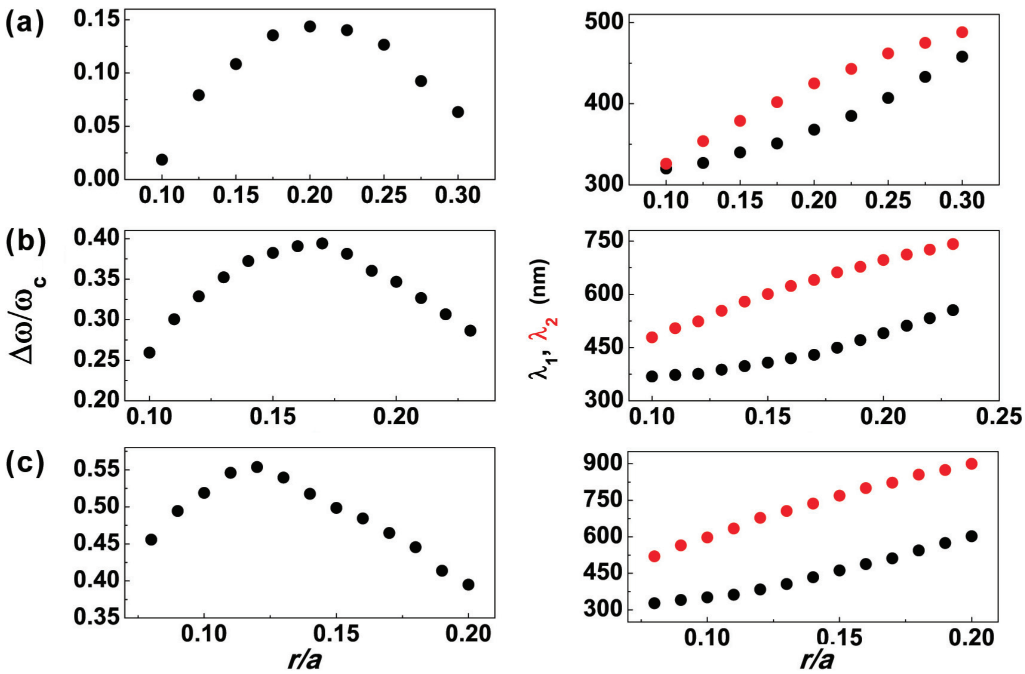

Figure 3. Gap–midgap ratio (left column) and band gap boundary wavelengths (right column) for an FPO distribution of cylinders in air as a function of the r/a ratio and for different refractive index contrasts Δn: 1 (**a**), 2.4 (**b**), 3.4 (**c**). The simulations have been performed for TM polarization.

FPO Pattern vs. HCP Pattern: TE case. It is well known [6], as we just verified above, that a proper two-dimensional distribution of high refractive index cylinders in a low refractive index environment leads to large TM PBGs. We can now analyze the complementary case where low refractive index (e.g., air) inclusions are distributed in a high refractive index medium, which favors the generation of wide TE PBGs.

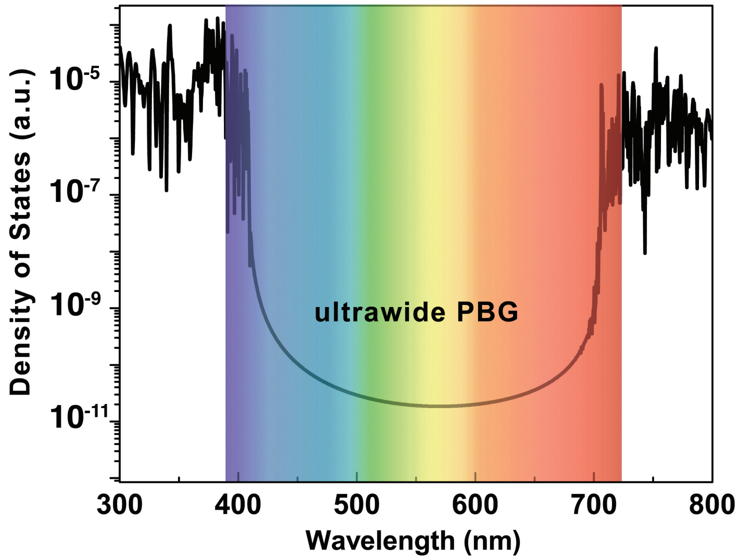

Figure 4. White band gap (WBG) for a blue-noise distribution of cylinders in air, obtained for $r/a = 0.13$ and TM polarization.

We compare our BND structure of circular holes with that formed by an HCP pattern of air inclusions in a high refractive index environment. In Figure 5, the gap–midgap ratios and corresponding band gap boundary wavelengths λ_1 and λ_2 are represented for both cases as a function of the r/a ratio and for a refractive index contrast of $\Delta n = 3.4$. Here, r stands for the radius of the holes while a represents the average minimum distance of a hole with respect to its neighbors (or simply the lattice constant in the HCP case). For FPO patterns, two white (all visible) PBGs take place, one for $r/a = 0.31$, spanning from $\lambda = 417$ nm to $\lambda = 770$ nm ($\Delta\omega/\omega_c = 59.5\%$), and the second for $r/a = 0.32$, spanning all the visible spectrum and including also a portion of the UVB spectral range ($\lambda_1 = 387$ nm; $\lambda_2 = 714$ nm; $\Delta\omega/\omega_c = 59.4\%$). On the other hand, the best performance, in terms of the gap–midgap ratio and for HCP patterns, is obtained for $r/a = 0.44$, leading to a PBG spanning a spectral range from 520 to 988 nm, with $\Delta\omega/\omega_c = 62\%$, which is comparable with the values obtained for a BND pattern. Furthermore, in this case, no WBG takes place: at most, the widest portion of the visible spectrum covered by a PBG is the one obtained for $r/a = 0.47$, with $\lambda_1 = 452$ nm, $\lambda_2 = 788$ nm, and $\Delta\omega/\omega_c = 54.1\%$.

PBG completeness. Now we can investigate the possible presence of complete PBGs in FPO patterns. As we stated above and as it is well known from literature [6], a two-dimensional PhC obtained with an HCP pattern of high refractive index cylinders in a low index environment (e.g., air) leads to large TM PBGs, which can be mainly explained by hopping between individual Mie resonators [11]. On the other hand, TE PBGs are favored in a connected lattice (e.g., HCP lattice of circular low index inclusions in a high index material), mainly because of Bragg-like multiple scattering phenomena.

Thus, one possible way to obtain complete PBGs in two-dimensional HCP patterns is to enlarge the radius of the low index inclusions in such a way that the spots between them look like localized connected regions of a high refractive index [6].

We analyzed the performance of this kind of optical configuration as a function of r/a, always in terms of $\Delta\omega/\omega_c$ (for both TM and TE polarizations) for $\Delta n = 3.4$. The obtained results are shown in Table 1. We can see how, for a proper choice of r/a, complete PBGs take place also for BND patterns. In particular, BND complete PBGs are generally larger than their periodic HCP counterpart, even for experimental feasible filling fractions ($r/a \sim 0.31$) (Figure 5). In more detail, the maximum value of the gap–midgap ratio for a complete PBG supported by a BND arrangement of holes ($\Delta\omega/\omega_c = 32.7\%$ for $r/a = 0.34$, with $\lambda_1 = 386$ nm and $\lambda_2 = 537$ nm) is considerably higher than the maximum one obtainable by a HCP structure ($\Delta\omega/\omega_c = 23.6\%$ for $r/a = 0.48$, with $\lambda_1 = 498$ nm and $\lambda_2 = 632$ nm). Examples of patterns supporting complete PGBs in the two different cases are reported in Figure 5.

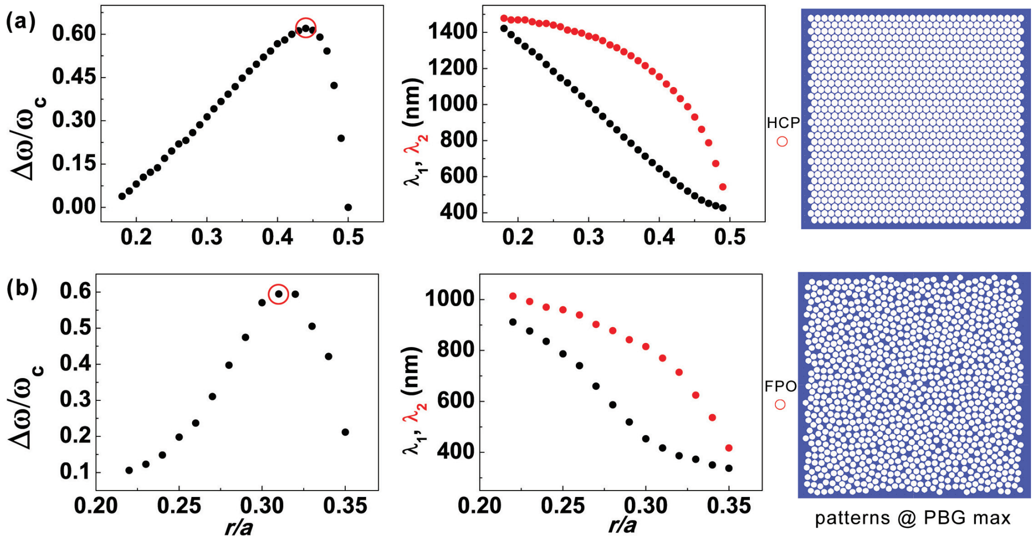

Figure 5. Gap–midgap ratio (left column) and band gap boundary wavelengths (center column) as a function of the r/a ratio for an HCP lattice of air holes in a high refractive index medium ($\Delta n = 3.4$) (**a**) and for FPO pattern of holes in the same medium (**b**), for TE polarization. On the right column, examples of HCP and FPO hole patterns supporting complete band gaps, respectively, for $r/a = 0.45$, with $\Delta\omega/\omega_c = 12.7\%$ and $r/a = 0.31$, with $\Delta\omega/\omega_c = 17.1\%$, as reported in Table 1. Red circles indicate the position of the considered patterns in the gap–midgap ratio curves.

Finally, it is worth noticing that the FPO complete PBGs are comparable with those of recently introduced hyperuniform disordered photonic structures [18,28], and that the FPO-based structure does not need tessellation (typically obtained by the proper interconnection of cylinders with a network of walls) in order to support both TM and TE band gaps, which represents an advantage when fabrication is involved for structures working in the visible-range scale.

Table 1. Complete PBG gap–midgap ratio $\Delta\omega/\omega_c$ for different values of r/a, in case of a distribution of air cylinders in a high refractive index medium ($\Delta n = 3.4$).

HCP-Pattern		FPO-Pattern	
r/a	$\Delta\omega/\omega_c$	r/a	$\Delta\omega/\omega_c$
0.45	12.7%	0.31	17.1%
0.46	16.3%	0.32	21.7%
0.47	19.9%	0.33	25.6%
0.48	23.6%	0.34	32.7%
0.49	19.3%	0.35	21.2%

2.3. Complex Waveguiding Pathways

As we mentioned above, isotropic PBGs allow one to design waveguides characterized by arbitrary bending angles or free-form defect pathways [40]. In periodic PhCs, indeed, the symmetry directions defined by the crystal itself impose well-defined bending angles [6], making easy to design, e.g., bends of 60° or 90° but strongly limiting other directions due to remarkable radiation losses. In Figure 6, the results of numerical simulations relative to different waveguides obtained after proper removal of scatterers in a FPO pattern of cylinders are shown.

The wavelengths of the propagating fields have been chosen as follows. After removal of cylinders along a desired path, a Gaussian time pulse excitation was launched at the inlet of the guide. The detection of the transmitted power by a monitor provided the peaks corresponding to the resonant modes of the waveguide (defect mode frequencies). Finally, the wavelength associated with the highest peak was used to launch a continuous wave field in the guide. The quality factor of the resonance measured the radiation loss in the waveguide. The quality factor was in the range $10^3 \div 10^5$ for all simulations. As can be seen from Figure 6, in addition to geometries easily obtainable also in periodic structures (straight guide excited at $\lambda = 445$ nm, right-angle guide excited at $\lambda = 621$ nm), the use of BND arrangements allows one to design circular waveguides ($\lambda = 479$ nm), the most significant example of a free-form pathway that reflects the statistically intrinsic isotropic nature of a blue-noise pattern.

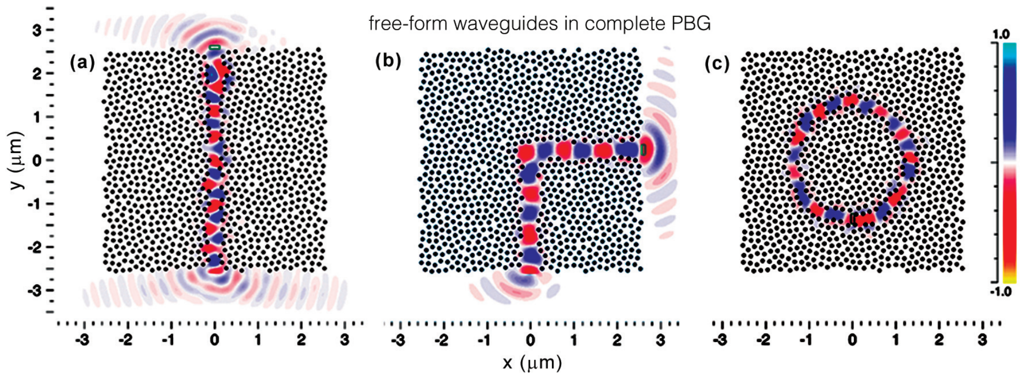

Figure 6. Electric field distributions in a linear (**a**), right-angle (**b**) and circular (**c**) waveguide obtained after proper removal of cylinders in the FPO pattern with $r/a = 0.13$. Excitation at $\lambda = 445$ nm (**a**), $\lambda = 621$ nm (**b**), and $\lambda = 479$ nm (**c**), and field source launched with TM polarization.

3. Conclusions

In conclusion, we show how farthest-point optimization, introduced and developed in the field of computer graphics in order to improve spatial dithering, represents an efficient method also in the design of photonic structures characterized by blue noise. The FPO-based disordered photonic structure studied here is able to support ultrawide, isotropic PBGs capable of covering the whole visible spectrum, with gap–midgap ratios overcoming those obtainable by quasi-periodic, aperiodic, and disordered structures introduced so far. In particular, the performances of FPO structures in terms of gap–midgap ratios are comparable to those obtainable by HCP patterns, and superior when referring to complete PBGs. In addition, complete PBGs in the FPO pattern can be achieved without domain tessellation. FPO patterns can be successfully fabricated in photolithographic masks or with electron beam lithography systems exploiting vector scan mode [41], as in all simulations the minimal spatial feature was of the order of 80 nm, well above nanofabrication potential limits. Of course, the intrinsic isotropy of the FPO PBGs enables rotational symmetries forbidden to periodic structures, making it possible to obtain free-form waveguides with arbitrary bending, as in the case of hyperuniform disordered photonic structures [40]. Several realizations of the blue-noise distributions using FPO gave basically the same results, and thus the system is stable against point pattern redistribution.The blue-noise disordered system studied here differs from a hyperuniform disordered structure in that only finite suppressed values of density fluctuations are achieved within a certain range of wavevectors. We conclude that the fluctuations must be suppressed only to a reasonable finite level of acceptance to induce the PBG opening, relaxing the stringent constraints imposed by zero density fluctuations, useful in particular for real-world realizations of such photonic structures.

Supplementary Materials: The following supporting information can be downloaded at https://www.mdpi.com/article/10.3390/opt4040042/s1: Figure S1: Statistical analysis of the spatial fluctuations of the FPO pattern.

Author Contributions: Conceptualization, E.D.T. and G.Z.; methodology, E.D.T.; formal analysis, E.D.T., S.R. and G.Z.; investigation, E.D.T. and G.Z.; writing—original draft preparation, E.D.T.; writing—review and editing, E.D.T., S.R. and G.Z.; visualization, S.R. and G.Z.; supervision, G.Z. All authors have read and agreed to the published version of the manuscript.

Funding: This research received no external funding.

Data Availability Statement: The data presented in this study are available on request from the corresponding author.

Conflicts of Interest: The authors declare no conflict of interest.

Abbreviations

The following abbreviations are used in this manuscript:

PBG	Photonic band gap
BND	Blue-noise disorder
HCP	Hexagonal close-packed
FPO	Farthest-point optimization
WBG	White band gap

References

1. Foresi, J.; Villeneuve, P.R.; Ferrera, J.; Thoen, E.; Steinmeyer, G.; Fan, S.; Joannopoulos, J.; Kimerling, L.; Smith, H.I.; Ippen, E. Photonic-bandgap microcavities in optical waveguides. *Nature* **1997**, *390*, 143. [CrossRef]
2. De La Rue, R.; Smith, C. Photonics: On the threshold of success. *Nature* **2000**, *408*, 653. [CrossRef] [PubMed]
3. Neumark, G.F.; Kuskovsky, I.L.; Jiang, H. *Wide Bandgap Light Emitting Materials and Devices*; John Wiley & Sons: Hoboken, NJ, USA, 2007.
4. Hou, S.; Xie, A.; Xie, Z.; Tobing, L.Y.; Zhou, J.; Tjahjana, L.; Yu, J.; Hettiarachchi, C.; Zhang, D.; Dang, C.; et al. Concurrent Inhibition and Redistribution of Spontaneous Emission from All Inorganic Perovskite Photonic Crystals. *ACS Photonics* **2019** , *6*, 1331–1337. [CrossRef]
5. Joannopoulos, J.D.; Villeneuve, P.R.; Fan, S. Photonic crystals: Putting a new twist on light. *Nature* **1997**, *386*, 143. [CrossRef]
6. Joannopoulos, J.; Johnson, S.; Winn, J.; Meade, R. *Photonic Crystals: Molding the Flow of Light*, 2nd ed.; Princeton University Press: Princeton, NJ, USA , 2011.
7. Cheung, S.K.; Chan, T.L.; Zhang, Z.Q.; Chan, C. Large photonic band gaps in certain periodic and quasiperiodic networks in two and three dimensions. *Phys. Rev. B* **2004**, *70*, 125104. [CrossRef]
8. Zoorob, M.; Charlton, M.; Parker, G.; Baumberg, J.; Netti, M. Complete photonic bandgaps in 12-fold symmetric quasicrystals. *Nature* **2000**, *404*, 740–743. [CrossRef]
9. Dal Negro, L.; Boriskina, S.V. Deterministic aperiodic nanostructures for photonics and plasmonics applications. *Laser Photonics Rev.* **2012**, *6*, 178–218. [CrossRef]
10. Fu, H.; Chen, Y.; Chern, R.; Chang, C.C. Connected hexagonal photonic crystals with largest full band gap. *Opt. Express* **2005**, *13*, 7854–7860. [CrossRef]
11. Sigmund, O.; Hougaard, K. Geometric properties of optimal photonic crystals. *Phys. Rev. Lett.* **2008**, *100*, 153904. [CrossRef]
12. Du, Q.; Faber, V.; Gunzburger, M. Centroidal Voronoi tessellations: Applications and algorithms. *SIAM Rev.* **1999**, *41*, 637–676. [CrossRef]
13. Zito, G.; Piccirillo, B.; Santamato, E.; Marino, A.; Tkachenko, V.; Abbate, G. FDTD analysis of photonic quasicrystals with different tiling geometries and fabrication by single-beam computer-generated holography. *J. Opt. A Pure Appl. Opt.* **2009**, *11*, 024007. [CrossRef]
14. Matarazzo, V.; De Nicola, S.; Zito, G.; Mormile, P.; Rippa, M.; Abbate, G.; Zhou, J.; Petti, L. Spectral characterization of two-dimensional Thue–Morse quasicrystals realized with high resolution lithography. *J. Opt.* **2010**, *13*, 015602. [CrossRef]
15. Zito, G.; Priya Rose, T.; Di Gennaro, E.; Andreone, A.; Santamato, E.; Abbate, G. Bandgap properties of low-index contrast aperiodically ordered photonic quasicrystals. *Microw. Opt. Technol. Lett.* **2009**, *51*, 2732–2737. [CrossRef]
16. Rose, P.; Zito, G.; Di Gennaro, E.; Abbate, G.; Andreone, A. Control of the light transmission through a quasiperiodic waveguide. *Opt. Express* **2012**, *20*, 26056–26061.
17. Zito, G.; Rusciano, G.; Sasso, A.; De Nicola, S. Symmetry-induced light confinement in a photonic quasicrystal-based mirrorless cavity. *Crystals* **2016**, *6*, 111. [CrossRef]
18. Florescu, M.; Torquato, S.; Steinhardt, P.J. Complete band gaps in two-dimensional photonic quasicrystals. *Phys. Rev. B* **2009**, *80*, 155112. [CrossRef]
19. Burresi, M.; Cortese, L.; Pattelli, L.; Kolle, M.; Vukusic, P.; Wiersma, D.S.; Steiner, U.; Vignolini, S. Bright-white beetle scales optimise multiple scattering of light. *Sci. Rep.* **2014**, *4*, 6075. [CrossRef]
20. Wilts, B.D.; Sheng, X.; Holler, M.; Diaz, A.; Guizar-Sicairos, M.; Raabe, J.; Hoppe, R.; Liu, S.H.; Langford, R.; Onelli, O.D.; et al. Evolutionary-Optimized Photonic Network Structure in White Beetle Wing Scales. *Adv. Mater.* **2018**, *30*, 1702057. [CrossRef]

21. Torquato, S.; Stillinger, F.H. Local density fluctuations, hyperuniformity, and order metrics. *Phys. Rev. E* **2003**, *68*, 041113. [CrossRef]
22. Florescu, M.; Torquato, S.; Steinhardt, P.J. Designer disordered materials with large, complete photonic band gaps. *Proc. Natl. Acad. Sci. USA* **2009**, *106*, 20658–20663. [CrossRef]
23. Hexner, D.; Levine, D. Hyperuniformity of critical absorbing states. *Phys. Rev. Lett.* **2015**, *114*, 110602. [CrossRef]
24. Hexner, D.; Chaikin, P.M.; Levine, D. Enhanced hyperuniformity from random reorganization. *Proc. Natl. Acad. Sci. USA* **2017**, *114*, 4294–4299. [CrossRef] [PubMed]
25. Froufe-Pérez, L.S.; Engel, M.; Damasceno, P.F.; Muller, N.; Haberko, J.; Glotzer, S.C.; Scheffold, F. Role of short-range order and hyperuniformity in the formation of band gaps in disordered photonic materials. *Phys. Rev. Lett.* **2016**, *117*, 053902. [CrossRef] [PubMed]
26. Kram, Y.A.; Mantey, S.; Corbo, J.C. Avian cone photoreceptors tile the retina as five independent, self-organizing mosaics. *PLoS ONE* **2010**, *5*, e8992. [CrossRef] [PubMed]
27. Jiao, Y.; Lau, T.; Hatzikirou, H.; Meyer-Hermann, M.; Corbo, J.C.; Torquato, S. Avian photoreceptor patterns represent a disordered hyperuniform solution to a multiscale packing problem. *Phys. Rev. E* **2014**, *89*, 022721. [CrossRef]
28. Man, W.; Florescu, M.; Williamson, E.P.; He, Y.; Hashemizad, S.R.; Leung, B.Y.; Liner, D.R.; Torquato, S.; Chaikin, P.M.; Steinhardt, P.J. Isotropic band gaps and freeform waveguides observed in hyperuniform disordered photonic solids. *Proc. Natl. Acad. Sci. USA* **2013**, *110*, 15886–15891. [CrossRef] [PubMed]
29. Schlömer, T.; Heck, D.; Deussen, O. Farthest-point optimized point sets with maximized minimum distance. In Proceedings of the ACM SIGGRAPH Symposium on High Performance Graphics, Vancouver, BC, Canada, 5–7 August 2011; ACM: New York, NY, USA, 2011; pp. 135–142.
30. Ulichney, R.A. Dithering with blue noise. *Proc. IEEE* **1988**, *76*, 56–79. [CrossRef]
31. Lau, D.L.; Ulichney, R.; Arce, G.R. Blue and green noise halftoning models. *IEEE Signal Process. Mag.* **2003**, *20*, 28–38. [CrossRef]
32. Balzer, M.; Schlömer, T.; Deussen, O. *Capacity-Constrained Point Distributions: A Variant of Lloyd's Method*; ACM: New York, NY, USA, 2009; Volume 28.
33. Atkinson, S.; Zhang, G.; Hopkins, A.B.; Torquato, S. Critical slowing down and hyperuniformity on approach to jamming. *Phys. Rev. E* **2016**, *94*, 012902. [CrossRef]
34. Kim, J.; Torquato, S. Effect of imperfections on the hyperuniformity of many-body systems. *Phys. Rev. B* **2018**, *97*, 054105. [CrossRef]
35. Lloyd, S. Least squares quantization in PCM. *IEEE Trans. Inf. Theory* **1982**, *28*, 129–137. [CrossRef]
36. Kim, J.; Torquato, S. New tessellation-based procedure to design perfectly hyperuniform disordered dispersions for materials discovery. *Acta Mater.* **2019**, *168*, 143–151. [CrossRef]
37. Zito, G.; Rusciano, G.; Pesce, G.; Malafronte, A.; Di Girolamo, R.; Ausanio, G.; Vecchione, A.; Sasso, A. Nanoscale engineering of two-dimensional disordered hyperuniform block-copolymer assemblies. *Phys. Rev. E* **2015**, *92*, 050601. [CrossRef] [PubMed]
38. Synopsys. FullWAVE Product Overview. 2019. Available online: https://www.synopsys.com/optical-solutions/rsoft/passive-device-fullwave.html (accessed on 1 June 2023).
39. Synopsys. BandSOLVE Product Overview. 2019. Available online: https://www.synopsys.com/optical-solutions/rsoft/passive-device-bandsolve.html (accessed on 1 June 2023).
40. Florescu, M.; Steinhardt, P.J.; Torquato, S. Optical cavities and waveguides in hyperuniform disordered photonic solids. *Phys. Rev. B* **2013**, *87*, 165116. [CrossRef]
41. De Tommasi, E.; Esposito, E.; Romano, S.; Crescitelli, A.; Di Meo, V.; Mocella, V.; Zito, G.; Rendina, I. Frontiers of light manipulation in natural, metallic, and dielectric nanostructures. *Riv. Nuovo Cimento* **2021**, *44*, 1–68. [CrossRef]